The Astronomical Journal, 166:213 (12pp), 2023 November https://doi.org/10.3847/1538-3881/acfed2

Reading Between the Lines: Investigating the Ability of JWST to Identify Discerning Features in exoEarth and exoVenus Transmission Spectra

Colby Ostberg[1], Stephen R. Kane[1], Andrew P. Lincowski[2,3], and Paul A. Dalba[4,5,6]
[1] Department of Earth and Planetary Sciences, University of California, Riverside, CA 92521, USA; costb001@ucr.edu
[2] Department of Astronomy and Astrobiology Program, University of Washington, Box 351580, Seattle, WA 98195, USA
[3] NASA NExSS Virtual Planetary Laboratory, Box 351580, University of Washington, Seattle, WA 98195, USA
[4] Department of Astronomy and Astrophysics, University of California, Santa Cruz, CA 95064, USA
[5] SETI Institute, Carl Sagan Center, 339 Bernardo Ave, Suite 200, Mountain View, CA 94043, USA
Received 2022 February 17; revised 2023 September 25; accepted 2023 September 30; published 2023 October 27

Abstract

The success of the Transiting Exoplanet Survey Satellite mission has led to the discovery of an abundance of Venus Zone terrestrial planets that orbit relatively bright host stars. Atmospheric observations of these planets play a crucial role in understanding the evolutionary history of terrestrial planets, past habitable states, and the divergence of Venus and Earth climates. The transmission spectrum of a Venus-like exoplanet can be difficult to distinguish from that of an Earthlike exoplanet however, which could severely limit what can be learned from studying exoVenuses. In this work we further investigate differences in transmission between hypothetical exoEarths and exoVenuses, both with varying amounts of atmospheric carbon dioxide (CO_2). The exoEarths and exoVenuses were modeled assuming they orbit TRAPPIST-1 on the runaway greenhouse boundary. We simulated James Webb Space Telescope Near-Infrared Spectrograph PRISM transit observations of both sets of planets between 0.6 and 5.2 μm, and quantified the detectability of major absorption features in their transmission spectra. The exoEarth spectra include several large methane (CH_4) features that can be detected in as few as six transits. The CH_4 feature at 3.4 μm is the optimal for feature for discerning an exoEarth from an exoVenus since it is easily detectable and does not overlap with CO_2 features. The sulfur dioxide (SO_2) feature at 4.0 μm is the best indicator of an exoVenus, but it is detectable in atmospheres with reduced CO_2 abundance.

Unified Astronomy Thesaurus concepts: Venus (1763); Exoplanet atmospheres (487); Exoplanets (498); Exoplanet atmospheric composition (2021); Transmission spectroscopy (2133); Observational astronomy (1145); Planetary science (1255)

1. Introduction

Despite its currently uninhabitable surface conditions, interest in Venus has been growing significantly over the past decade. This is due in part to realizations regarding the importance of Venus to planetary habitability (Kane et al. 2019), whether it maintained a temperate climate up to ~0.7 Gya (Way et al. 2016; Way & Del Genio 2020), or was unable to condense surface liquid water after its magma-ocean phase (Hamano et al. 2013; Turbet et al. 2021). The ambiguity regarding the evolution of Venus through time makes its current environment even more intriguing and further illustrates the need to understand why the climate of Venus may have diverged so drastically from Earth. The next generation of Venus missions such as the Deep Atmosphere Venus Investigation of Noble gases, Chemistry, and Imaging (Garvin et al. 2022); Venus Emissivity, Radio Science, InSAR, Topography, and Spectroscopy (Cascioli et al. 2021); and EnVision (Ghail et al. 2017) missions will be crucial for understanding Venus' history by constraining its water-loss history, determining the extent of geological activity, and providing insight into its interior structure.

A complimentary approach to studying possible evolutionary pathways of Venus is through the study of Venus-like exoplanets. Due to the intrinsic bias of the transit method toward smaller star–planet separations (Kane & von Braun 2008), the Kepler and Transiting Exoplanet Survey Satellite (TESS; Ricker et al. 2015) missions have discovered a plethora of terrestrial exoplanets with orbits in the Venus zone (VZ; Kane et al. 2014; Ostberg & Kane 2019; Ostberg et al. 2023). The TESS VZ planets are of particular interest as their host stars are much brighter than those of Kepler planets, making TESS planets more amenable to atmospheric spectroscopy with the James Webb Space Telescope (JWST) or other future facilities (Louie et al. 2018; Stassun et al. 2019). Various studies have modeled the transmission spectra of potential exoVenuses and predicted the efficiency at which JWST could observe them (e.g., Ehrenreich et al. 2012; Lincowski et al. 2018; Lustig-Yaeger et al. 2019a, 2019b; Way et al. 2023). Obtaining information from an exoVenus atmosphere will be a challenging endeavor however, as Venus-like clouds and hazes may prevent the detection of molecular species, or an atmosphere at all (e.g., Ehrenreich et al. 2006; Fauchez et al. 2019; Barstow 2020; Komacek et al. 2020). In addition, it has been demonstrated that retrieval algorithms have difficulty discerning an Earthlike transmission spectrum from a Venus-like spectrum (Barstow et al. 2016). The inability to confidently identify an exoVenus or exoEarth will hinder efforts to learn the primary factors for Venus developing uninhabitable conditions, which is essential for understanding the circumstances which lead to the development of habitable worlds.

[6] Heising-Simons 51 Pegasi b Postdoctoral Fellow.

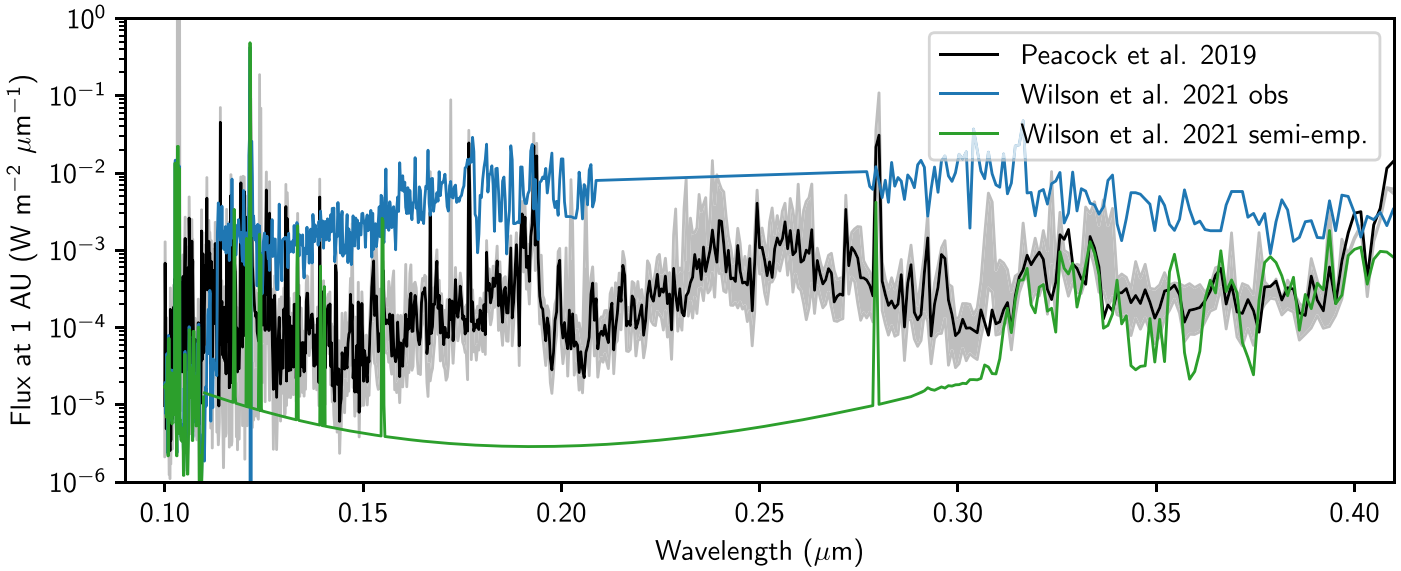

Figure 1. A comparison of three TRAPPIST-1 spectra in the UV. The black line is the average of three spectra simulated by Peacock et al. (2019), and is the spectrum used in the VPL Climate simulations. Both the blue and green lines are spectra from Wilson et al. (2021), and were produced using observational data and a semiempirical model, respectively.

In this work we present an analysis of both hypothetical exoEarth and exoVenus transmission spectra with varying atmospheric CO_2 abundance to investigate potential pathways to differentiating the two planets. This entails determining the key spectral differences between an exoEarth and exoVenus and quantifying the detectability of the unique features in each planets' spectra. In Section 2 we describe the climate model used to produce the exoEarth and exoVenus atmospheres, the process of simulating transmission spectra from the model output, and how we quantified the detectability of absorption features. Section 3 goes into detail about the detectability of all major absorption features in the transmission spectra of both planet types, and how their detectability changes as a function of atmospheric CO_2 abundance. In Section 4 we discuss the features which are unique to each planets' spectra, the type of observing proposal that would be required to detect them, and the caveats of our analysis. Lastly, Section 5 includes a summary of the main results and concluding remarks.

2. Methods

2.1. Modeling ExoEarth and ExoVenus Atmospheres

To generate model atmospheres for Venus-like and Earthlike conditions, we followed the methods and models of Lincowski et al. (2018) and Meadows et al. (2023), respectively. As in those works, we used VPL Climate, a layer-by-layer, spectrum-resolving 1D climate model, which uses mixing length theory and latent heat exchange where appropriate to time-step a temperature profile to radiative-convective equilibrium (Lincowski et al. 2018; Robinson & Crisp 2018). The inputs required for VPL Climate are described in the respective model papers, and summarized below.

For radiative transfer, VPL Climate uses the Spectral Mapping Atmospheric Radiative Transfer (SMART) model, which is an accurate, spectrum-resolving radiative transfer model (Meadows & Crisp 1996; Crisp & Titov 1997), and has been successfully applied to both Earth (Crisp & Titov 1997; Robinson et al. 2011) and Venus (Meadows & Crisp 1996; Arney et al. 2014; Lincowski et al. 2021). SMART uses the Discrete Ordinate Radiative Transfer (Stamnes et al. 1988, 2000) solver to calculate the radiation field. SMART uses LBLABC (Crisp 1997) to compute line-by-line absorption coefficients, and resolves both water (H_2O) and CO_2 line wings to 1000 cm^{-1}. The extensive Ames line list (Huang et al. 2017) is used for CO_2 for the exoVenuses, HITEMP2010 (Rothman et al. 2010) is used for H_2O and CO for the exoVenuses, and HITRAN2016 (Gordon et al. 2017) is used for the remaining gases and for the exoEarths. LBLABC includes self and foreign line broadening. SMART uses laboratory-measured collision-induced absorption for CO_2–CO_2, O_2–O_2, and N_2–N_2, and ultraviolet (UV) cross sections as necessary (see Lincowski et al. 2018 for a description of those data sources). For the exoEarths, moist convection is obtained through mixing length theory and latent heat release. Meadows et al. (2023, in preparation) showed that this, coupled with the photochemistry model, faithfully reproduces the global conditions of Earths atmosphere. In both cases, VPL Climate was coupled to the photochemical component of Atmos, as described in Lincowski et al. (2018) and Meadows et al. (2023).

Aerosols and clouds are included in the VPL Climate simulations. For the exoEarths, we used standard Earth stratocumulus (water) and cirrus (water-ice) clouds to obtain the global surface temperature. The stratocumulus clouds were defined to be between 0.827 and 0.900 bars, and the cirrus clouds are between 0.257 and 0.331 bars. The clouds were described in Meadows et al. (2023, in press) and derive from Earth atmospheric observations (Robinson et al. 2011). For exoVenuses, we generate optical depths and aerosol properties converted from monodisperse, layer-by-layer sulfuric acid (H_2SO_4) aerosols generated in the photochemical code. These aerosols vary in particle size and H_2SO_4 fraction. A more detailed description of the H_2SO_4 aerosols can be found in Lincowski et al. (2018).

The exoEarths and exoVenuses were both modeled as 1 $M_\oplus$, 1 $R_\oplus$ planets, near the runaway greenhouse limit for TRAPPIST-1. We chose TRAPPIST-1 as the host star since the majority of exoplanets are being discovered around cooler M-type stars. For both photochemical and climate modeling,

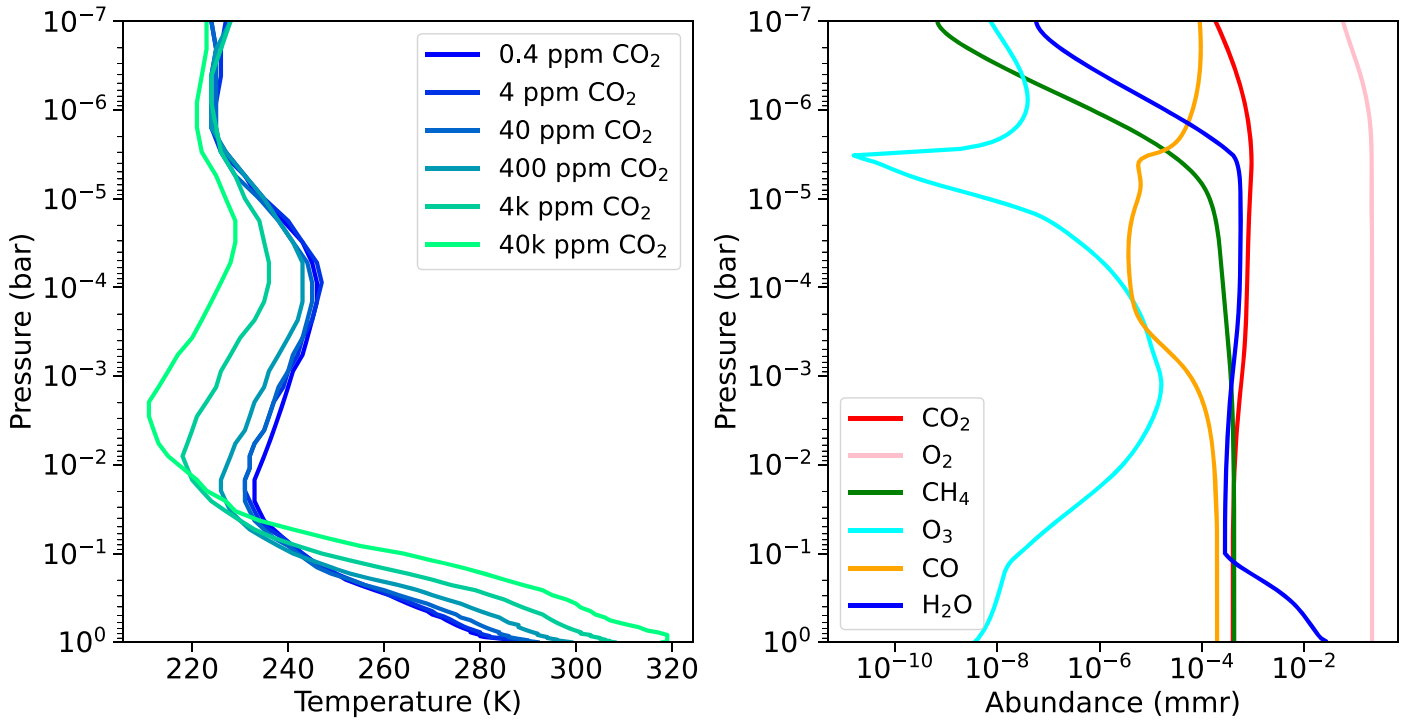

Figure 2. The TP profiles for the six exoEarth atmospheres (left panel) and the chemical abundance profiles for the 400 ppm exoEarth (right panel).

we used a version of the Peacock et al. (2019) synthetic spectrum calibrated to GALEX near-ultraviolet (NUV) and far-ultraviolet (FUV) fluxes. Figure 1 shows the (Peacock et al. 2019) spectrum in comparison to two spectra from Wilson et al. (2021), in units of specific flux converted to SI units at 1 au. The Peacock et al. (2019) spectrum, which had spurious lines removed, is an average of the three spectra simulated by Peacock et al. (2019), the range of which are shaded in gray. We also plot the Hubble Space Telescope (HST) Cosmic Origins Spectrograph (COS) observations published by Wilson et al. (2021) in blue, which is missing a segment of data between approximately 0.2 and 0.3 μm. For planetary modeling, as we conduct here, Wilson et al. (2021) recommended using their semiempirical model, which is plotted in green. The semiempirical model replaces essentially the entire critical NUV and FUV flux range with a polynomial fit. In our opinion, this is insufficient for planetary modeling, given that Peacock et al. (2019) conducted a careful UV spectral model, which covers this range. As can be seen in Figure 1, the Peacock et al. (2019) model lies largely in between the low flux of the semiempirical model and the flux observed by HST COS. Peacock et al. (2019) noted their models were representative of upper limits as observed by GALEX in the NUV and FUV bands, the spectrum shown is still lower than the HST COS observations. Wilson et al. (2021) had recommended to not use the observed spectrum, due to low S/N of M dwarf UV observations, particularly for TRAPPIST-1. Although individual strong line fits may be poor according to Wilson et al. (2021), the integrated flux throughout the FUV and NUV is important for planetary photochemical modeling. Therefore, we use the averaged Peacock et al. (2019) spectrum in our climate models.

To accommodate varying CO_2 levels, N_2 was exchanged for CO_2 to keep the surface pressure as 1 bar for the exoEarths, and 10 bar for the exoVenuses. The exoEarth atmospheres are composed of H_2O, CO_2, ozone (O_3), nitrous oxide (N_2O), carbon monoxide (CO), methane (CH_4), oxygen (O_2), sulfur dioxide (SO_2), carbonyl sulfide (OCS), ethane (C_2H_6), dimethyl sulfide (C_2H_6S), hydrogen chloride (HCl), and chloromethane (CH_3Cl). The exoVenuses have atmospheres made of H_2O, CO_2, CO, SO_2, OCS, O_2, HCl, and H_2SO_4. The exoEarths used the average surface albedo for Earth (Meadows et al. 2018) and the exoVenuses used a basalt surface (Lincowski et al. 2018). The resulting temperature-pressure (TP) profiles for all exoEarth and exoVenus cases are shown in Figures 2 and 3.

2.2. PSG and PandExo

The transmission spectra for the exoEarths and exoVenuses were modeled using the Planetary Spectrum Generator (PSG; Villanueva et al. 2018). PSG is a publicly available online interface that couples radiative transfer models with planetary and spectral databases. PSG requires input which describes the host star, planet, orbital configuration, and the observing instrument. The host star used was TRAPPIST-1, and all exoEarth and exoVenus were defined to have 1 $M_\oplus$, 1 $R_\oplus$, and a semimajor axis on the runaway greenhouse boundary (0.02393 au; Kopparapu et al. 2013, 2014). The observing instrument used in the PSG simulations was JWST Near-Infrared Spectrograph (NIRSpec) PRISM, which has a bandpass of 0.6–5.3 μm. The atmospheres for the exoEarths and exoVenuses were defined using the TP and molecular abundance profiles from the Atmos simulations. Both cloudy and clear-sky transmission spectra were produced for each planet. We did not include emission spectra since secondary eclipse observations are typically used for detecting the presence of atmospheres and not specific molecules, as was done with TRAPPIST-1 b (Greene et al. 2023) and TRAPPIST-1 c (Zieba et al. 2023).

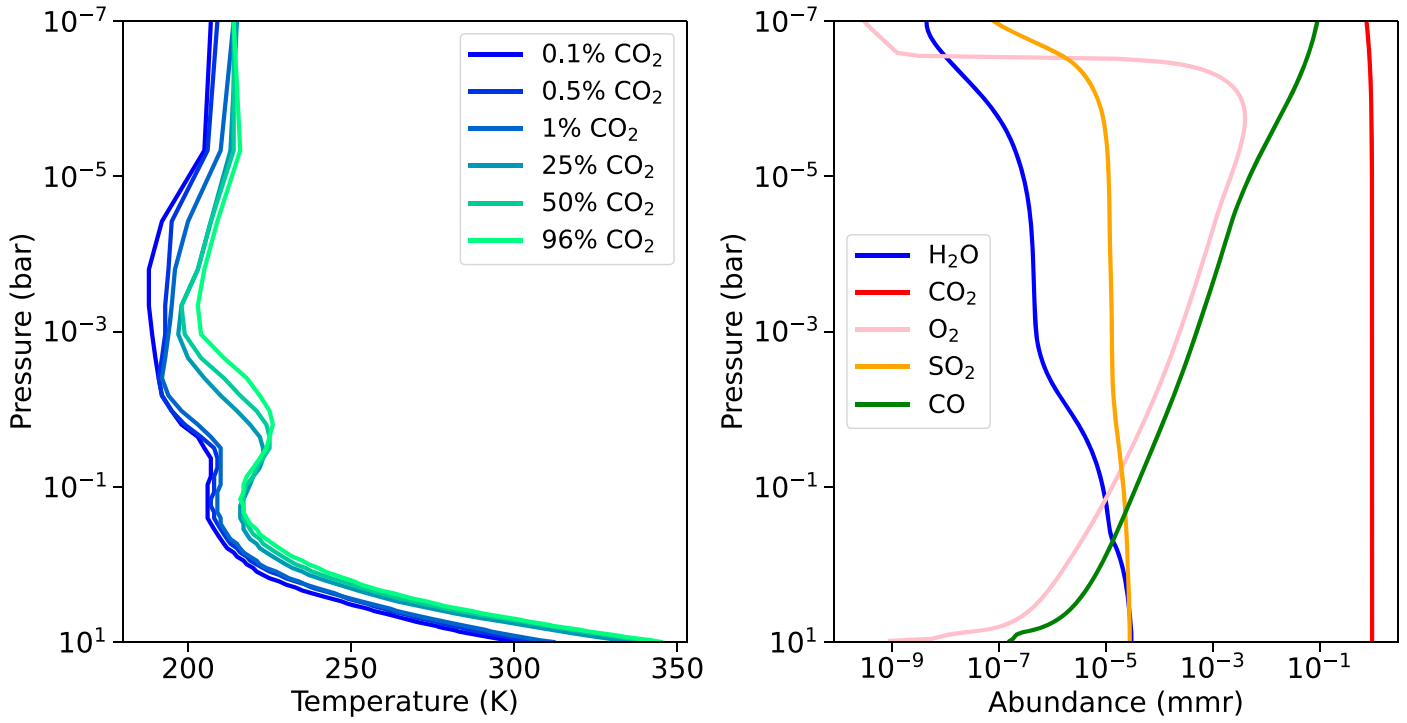

Figure 3. The TP profiles for the six exoVenus atmospheres (left panel) and the chemical abundance profiles for the 96% CO_2 exoVenus (right panel).

The upper panel of Figure 4 shows the PSG transmission spectra for all six exoEarths assuming clear-skies. Increasing CO_2 abundance has little effect on the exoEarth spectra until the abundance reaches 4 k ppm CO_2. In the 4 k and 40 k ppm CO_2 spectra, the 2.0 and 2.7 μm CO_2 features become visible. The 4.3 μm CO_2 feature is visible in every CO_2 case, but only increases in size in the 4 k and 40 k ppm cases. All other features are primarily composed of either H_2O or CH_4, and their size remains constant in all cases. The modeled exoEarth atmospheres have greater CH_4 absorption than Earth because the spectral energy distribution of TRAPPIST-1 enhances the production of CH_4 (Meadows et al. 2018). Other molecules with smaller contributions to the exoEarth absorption features include CO and N_2O (Figure 5). The lower panel of Figure 4 displays the effect of water and water-ice clouds on the 0.4 and 40 k ppm exoEarth transmission spectra. Since the clouds are located at low altitudes they have little effect on the spectra, and only slightly raise the continuum at wavelengths less than 2.3 μm.

The exoVenus spectra have far more variation with changing CO_2 abundance since majority of its features are composed of only CO_2 absorption (Figure 6). The only other prominent molecular absorption is caused by sulfur dioxide (SO_2) at 4.0 μm and CO at 4.6 μm. In the clear-sky exoVenus spectra, the SO_2 feature is only visible in lower CO_2 cases. In the higher CO_2 atmospheres the SO_2 feature is concealed because of increased atmospheric scale height and increased CO_2 absorption (Figure 7). Larger CO_2 abundance does not equate to larger CO_2 features in the 50% and 96% CO_2 cases due to an increase in scale height, which compresses the atmosphere and reduces the size of absorption features. As a result, the 50% and 96% CO_2 exoVenus spectra have features similar in size to that of the 0.1% CO_2 spectrum. The scale height and CO_2 absorption in the 25% CO_2 spectrum are optimal, allowing it to have the largest features of the six exoVenuses.

Unlike the clouds in the exoEarth spectra, the H_2SO_4 haze in the exoVenus spectra significantly impacts the size of absorption features (Figure 6). The haze causes the CO_2 feature at 1.7 μm to be entirely muted, and the CO_2 feature at 2.0 μm is only slightly visible. In the 0.1% CO_2 cloudy spectrum, both the 2.7 μm CO_2 feature and 4.0 μm SO_2 feature are reduced to a height of about 10 ppm. The 4.3 μm CO_2 is more resilient to the haze, and maintains a height of about 20 and 40 ppm in the 0.1% and 96% CO_2 spectra, respectively.

The transmission spectra in Figure 6 were used as inputs for PandExo (Batalha et al. 2017) to simulate observations with JWST NIRSpec PRISM. PandExo utilizes the Space Telescope Science Institute's Exposure Time Calculator (ETC) and Pandeia (Pontoppidan et al. 2016) to model instrumental and background noise sources. The physical and orbital parameters for the planet and host star were defined in PandExo to be the same values used for PSG. The atmosphere of the host star is generated by PandExo using the Phoenix Stellar Atlas (Husser et al. 2013), and each planets' atmosphere was defined by their PSG transmission spectrum.

NIRSpec PRISM was defined to have a saturation level of 80% a full well (Greene et al. 2016), and the noise floor was set to 5 ppm to reflect the noise seen in recent NIRSpec observations (Lustig-Yaeger et al. 2023). The ratio of in-transit to out of transit observing time was set to 1, making a single transit observation equivalent to 1.75 hr of observation, assuming no overhead time. We use the SUB512 subarray with six groups per integration and the native binning of NIRSpec PRISM ($R = 100$). An example of PandExo simulated JWST data assuming 15 transit observations of both the 400 ppm CO_2 exoEarth and 96% CO_2 exoVenus are shown in Figure 8. The simulated data has worse uncertainty and spectral resolution at longer wavelengths because of the sensitivity of NIRSpec PRISM. This causes the JWST data to resolve less of

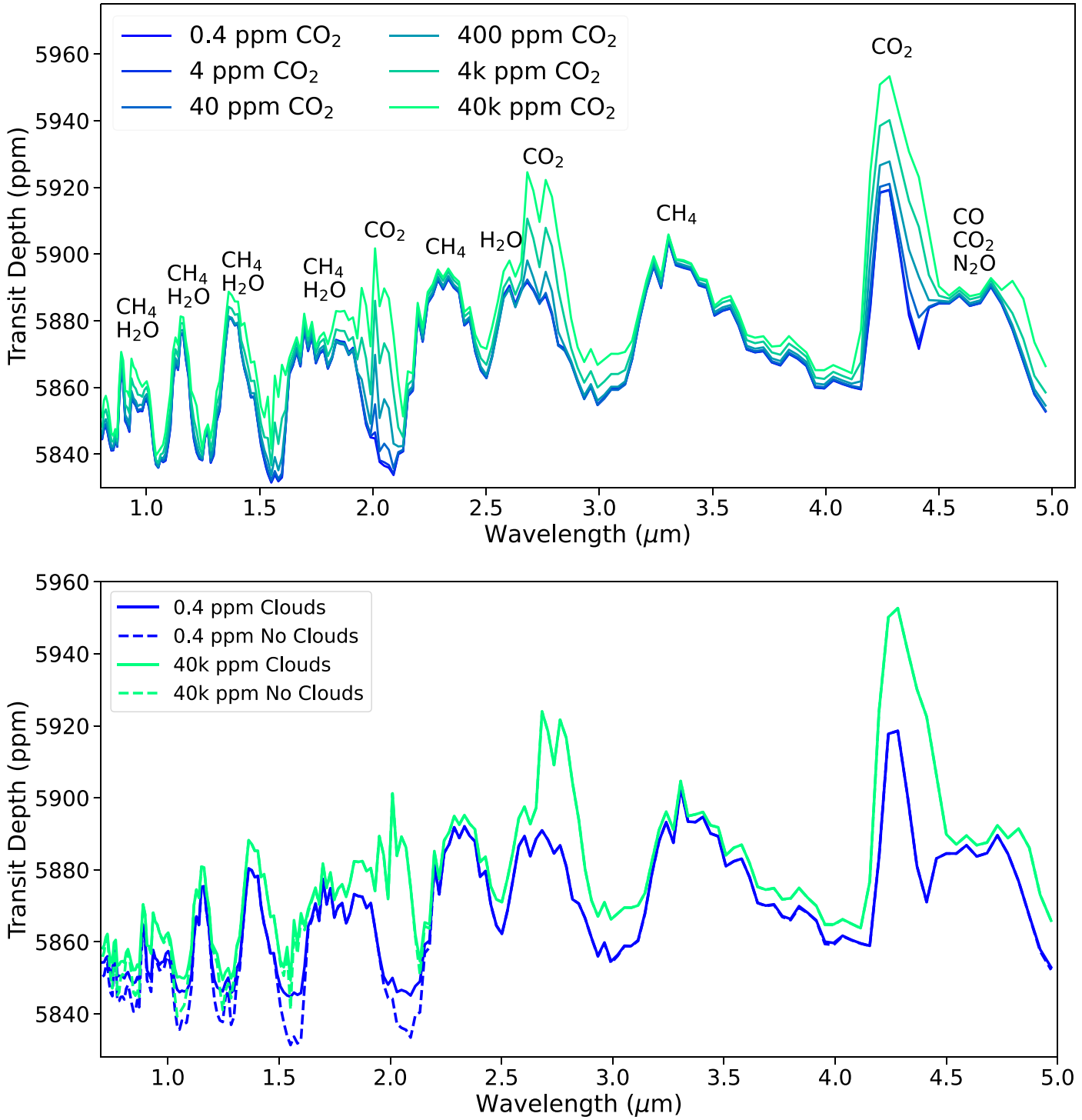

Figure 4. The transmission spectra of the six clear-sky TRAPPIST-1 exoEarths from the VPL Climate simulations (upper panel), and transmission spectra with and without clouds for the 0.4 and 40 k ppm CO_2 exoEarths. Absorption features are labeled with the molecules which contribute the most absorption. Features labeled with multiple molecules consist of more than one primary absorber.

the 4.3 μm feature than the features at shorter wavelengths, despite the 4.3 μm feature being larger.

2.3. Determining the S/N of Absorption Features

We calculated the S/N of prominent absorption features in the exoEarth and exoVenus transmission spectra in order to quantify their detectability. The χ^2 approach used by Lustig-Yaeger et al. (2019a) was adopted for our S/N calculations:

$$S/N = \sqrt{\sum_{i}^{N_{\lambda_i}} \left(\frac{y_i - y_{\text{cont}}}{\sigma_i} \right)^2}. \quad (1)$$

In Equation (1), y_i is the i'th y value of the model spectrum within the wavelength range of a feature, σ_i is the corresponding uncertainty of the simulated JWST data from PandExo,

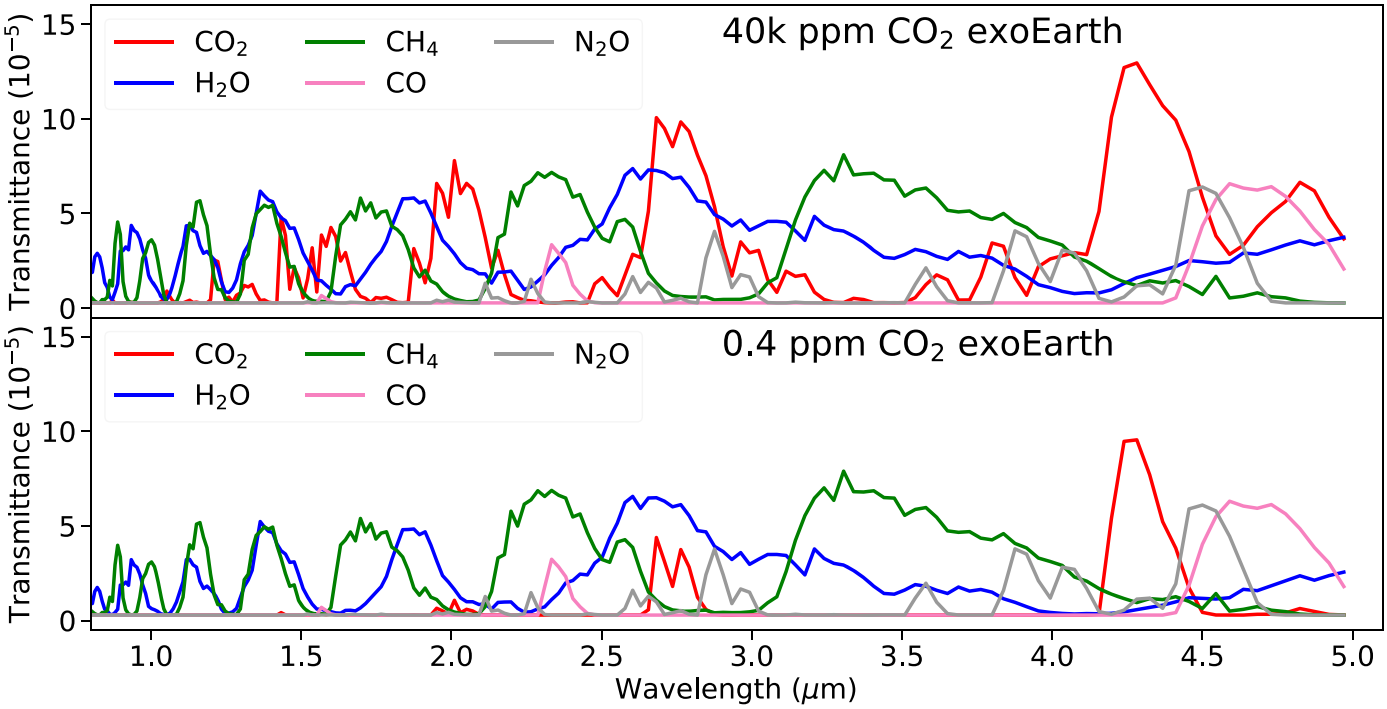

Figure 5. The transmittance of each molecular species in the 40 k ppm (upper panel) and 0.4 ppm (lower panel) CO_2 exoEarth atmospheres. Absorption by CO_2 is much stronger in the 40k ppm exoEarth, but all other molecular absorption remains constant in both cases.

and y_{cont} is the continuum, which we defined as the minimum value of the entire spectrum.

The S/N of a given feature is first calculated for a single transit observation, and a scaling relationship is used to interpolate the S/N to up to 100 transits. We then determined the number of transits required for a feature to reach a S/N $\geqslant$5, which is the detectability threshold used in previous studies (e.g., Lustig-Yaeger et al. 2019a; Pidhorodetska et al. 2020; Felton et al. 2022). If the threshold is not reached within 100 transit observations then the feature is determined to be undetectable. Since more complex retrieval models will be required to confirm the presence of molecular species from actual JWST data, we acknowledge that the values for S/N and number of transits that we report are to be considered upper and lower limits, respectively.

We chose to focus on 10 features in the exoEarth spectra and 7 in the exoVenus spectra, which are labeled in Figures 4 and 6. For reference, the defined wavelength ranges and molecular absorbers for every feature in the exoEarth and exoVenus spectra are listed in Tables 1 and 3, respectively. The number of transits required to detect every feature in the exoEarth and exoVenus spectra were calculated using Equation (1), and the results are discussed in Section 3.

3. Results

Using Equation (1) we determined the number of transit observations required to detect the 10 absorption features in the exoEarth transmission spectra and seven features in the exoVenus spectra. Shown in Table 1 are the number of transits required for the features in the six clear-sky exoEarth cases to reach the S/N threshold. The CH_4 feature at 0.9 μm is the smallest of the features and therefore requires the most time to detect. The size of the CH_4 and H_2O features did not change with increasing CO_2 (Figure 4), causing the number of transits required to detect to remain relatively constant across all CO_2 cases. The CO_2 features at 2.0, 2.7, and 4.3 μ only grew in size when CO_2 was increased to 4 k and 40 k ppm. This caused the number of transits required for detection of these features to be relatively unchanged in all but the 4 k and 40 k ppm CO_2 exoEarth cases. The CO_2 feature at 2.0 μm is undetectable when CO_2 abundance is less than 4 k ppm. The CH_4 features at 1.7, 2.3, and 3.5 μm are are the most consistently detectable features in the exoEarth spectra as they can be detected in at least nine, seven, and six transits, respectively. Table 2 lists the number of transits required to detect features in the cloudy exoEarth transmission spectra. Since clouds have a negligible effect on the exoEarth spectra (Figure 4), the required transits are the same for both the cloudy and clear-sky spectra.

The number of transits required for the absorption features in the clear-sky exoVenus spectra to reach the S/N threshold are shown in Table 3. The 25% CO_2 case requires the least amount of transits to detect all CO_2 features, whereas the 0.5% and 1% CO_2 atmospheres are the best opportunity to detect SO_2. The large CO_2 feature at 4.3 μ requires a similar amount of transits to be detected in the 96% and 0.1% CO_2 cases because the increased scale height of the 96% CO_2 atmosphere reduces the features size. The CO_2 features at 2.0 and 2.7 μm require far less transits to be detected in the 96% CO_2 case than in the 0.1% CO_2 case however, since these features are only prominent in atmospheres with high CO_2 abundance. The SO_2 feature at 4.0 μm is the only feature that is not also present in the exoEarth spectra; however, it requires a minimum of 47 transits to be detected, and becomes undetectable in the 96% CO_2 case. Alternatively, the CO_2 feature at 1.6 μm does not become detectable until there is at least 25% atmospheric CO_2. The smallest CO_2 feature at 1.3 μm cannot be detected in less than 100 transit observations for any of the six exoVenuses.

Table 4 lists the amount of transits required to detect the features in the hazy exoVenus spectra. The haze prevents all

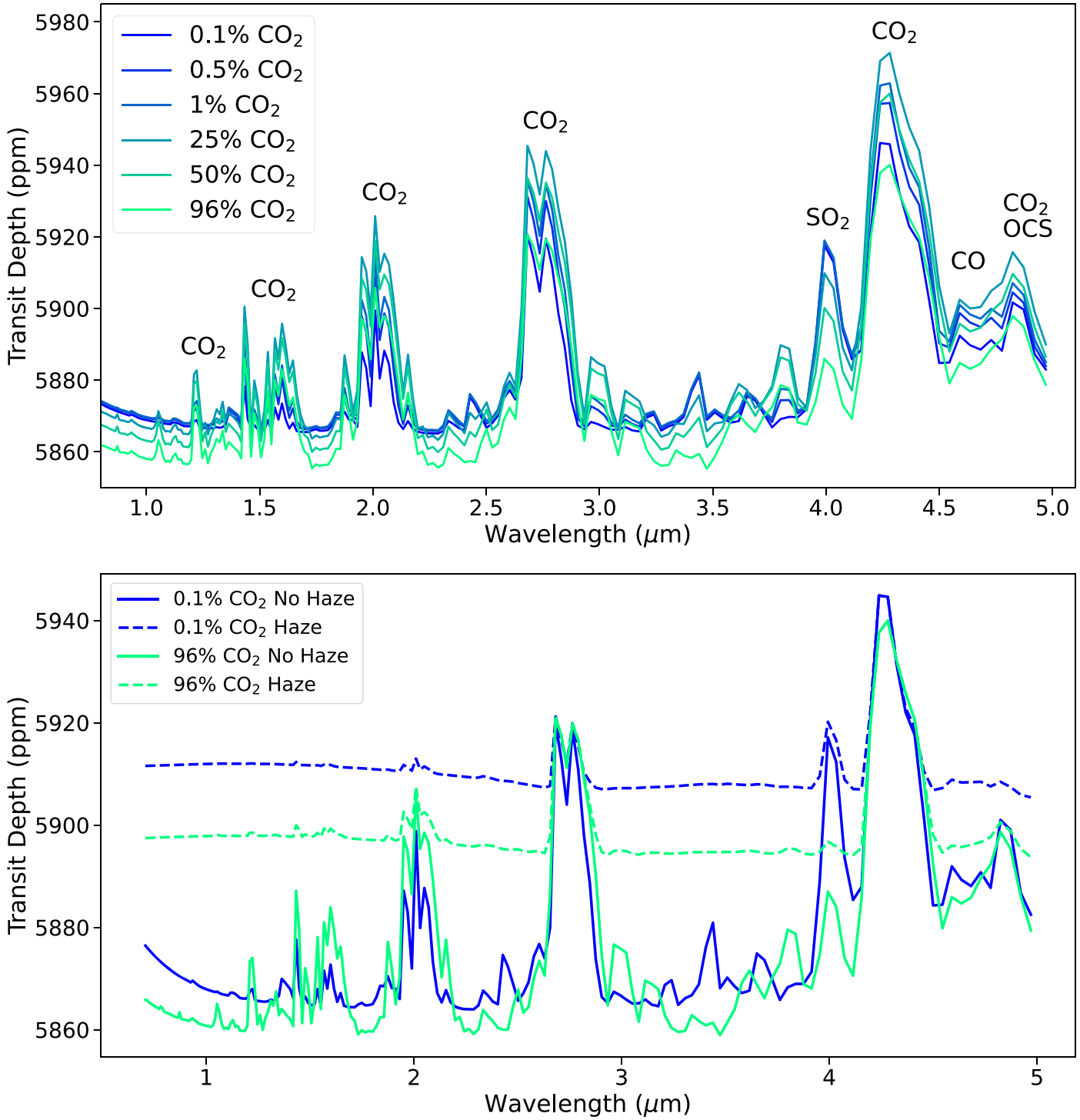

Figure 6. The transmission spectra of the six clear-sky TRAPPIST-1 exoVenuses from the VPL Climate simulations (upper panel), and transmission spectra with and without haze for the and 0.1% and 96% CO_2 exoVenuses (lower panel). Absorption features are labeled with the molecules which contribute the most absorption. Features labeled with multiple molecules consist of more than one primary absorber.

but the 2.7 and 4.3 μ CO_2 features from being detected in any of the six exoVenus spectra. The 4.3 μ feature is detectable in as little as 33 transits in the 25% CO_2 case, but can also become undetectable in the lowest CO_2 case. The 2.7 μm feature would require a minimum of 66 hr to detect. The haze concealing SO_2 absorption is particularly significant given that it is the only feature unique to the exoVenus spectra, and leads to ambiguity when using retrieval algorithms to derive surface conditions from the spectrum (Barstow et al. 2016).

4. Discussion

4.1. Features to Prioritize in Observations

If the goal of an observation is to solely detect molecular absorption in an atmosphere, then the 4.3 μm CO_2 feature is likely the best option for both an exoEarth and exoVenus. The feature can be detected in as little as 10 transits in the clear-sky exoEarth and clear-sky exoVenus spectra, and remains detectable with lower atmospheric CO_2 and when clouds or

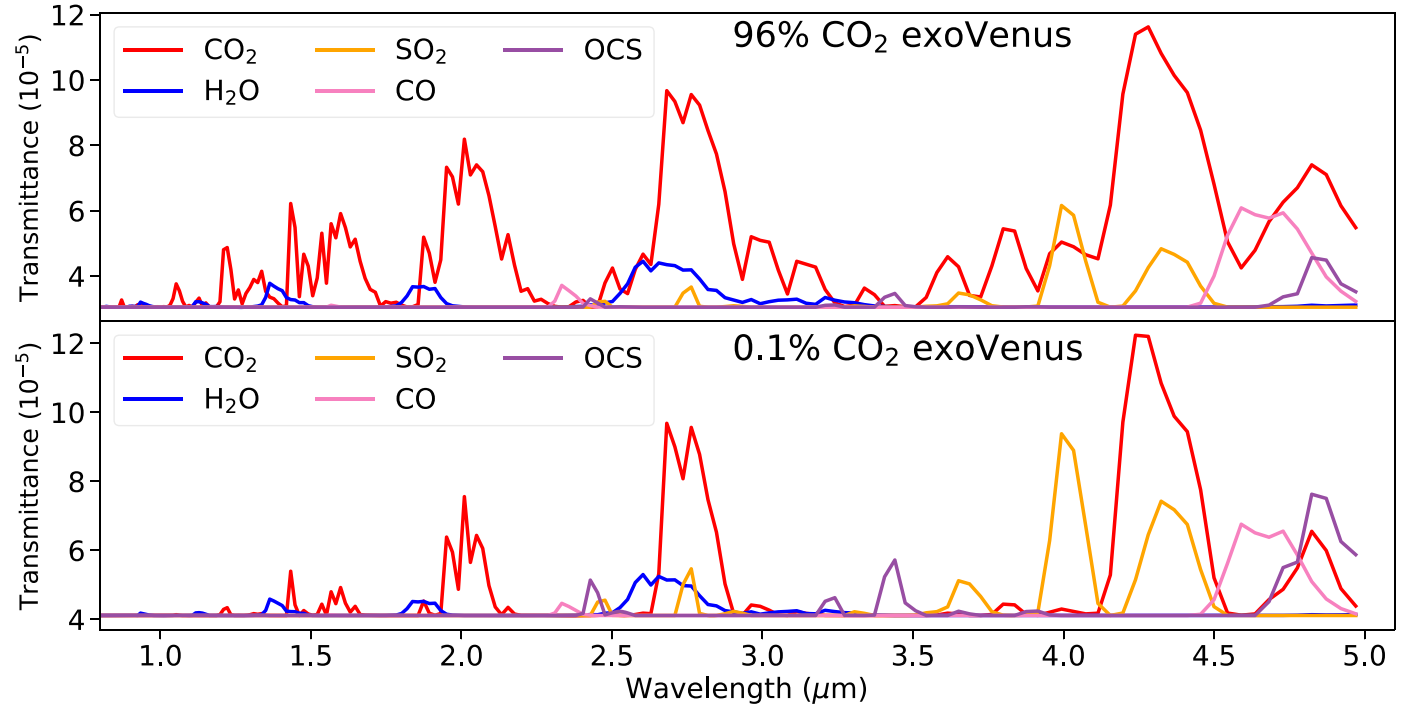

Figure 7. The transmittance of each molecular species in the 96% (upper panel) and 0.1% (lower panel) CO_2 exoVenus atmospheres. The decreased CO_2 absorption in the 0.1% CO_2 case allows for more absorption by the SO_2 feature at 4.0 μm.

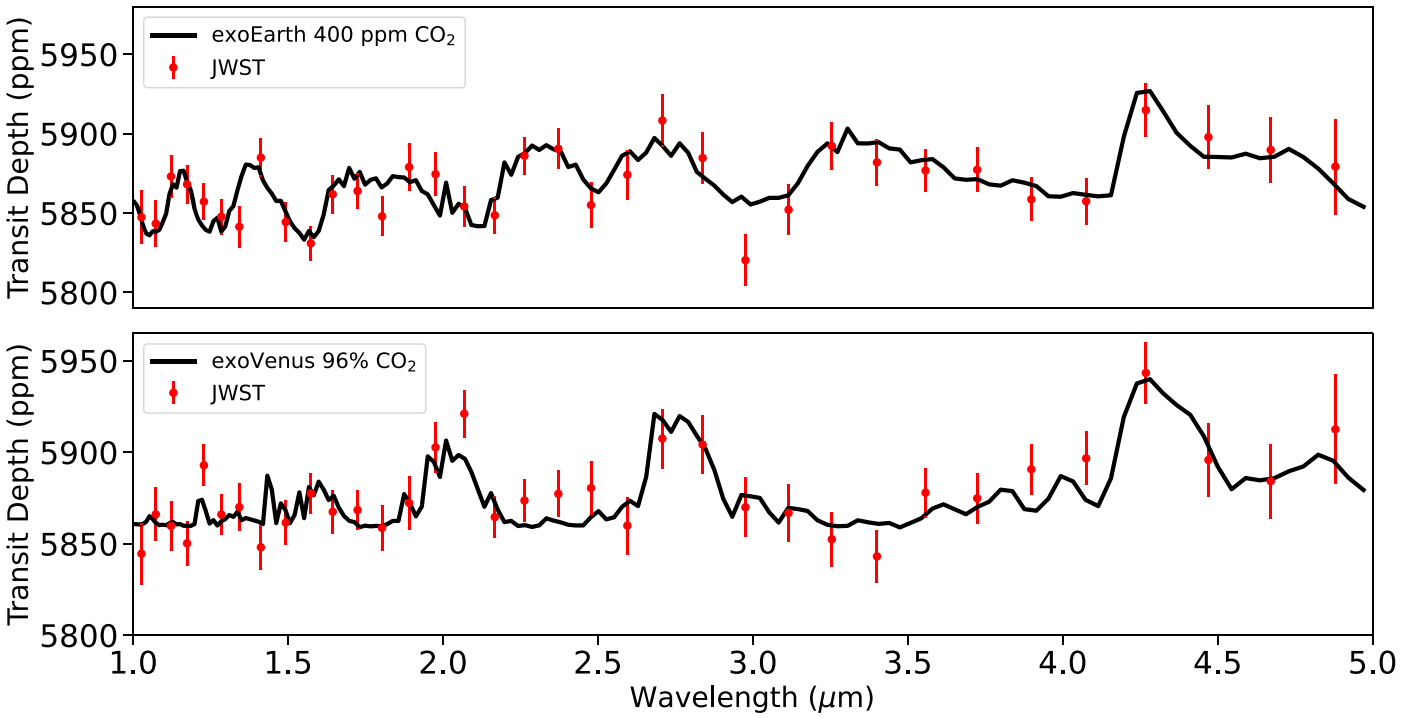

Figure 8. Simulated JWST NIRSpec PRISM spectroscopy data from 15 transit observations of the 400 ppm CO_2 exoEarth (top) and 96% CO_2 exoVenus (bottom), both without clouds or hazes. The JWST data was binned down to a resolving power of $R = 12$ for easier visibility.

haze are present (Figures 4 and 6). Beyond just confirming the presence of CO_2, the CO_2 features at 1.7, 2.0, and 2.7 μm are useful for estimating CO_2 abundance. These features only become present in the transmission spectra of atmospheres with high CO_2 abundance, whereas the 4.3 μm feature is visible even in the lowest CO_2 cases for both planets (Figures 4 and 6). In theory, these features would be useful for estimating whether a planet has a Venus-like or Earthlike amount of atmospheric CO_2, and in turn whether the planet may be habitable. The issue however is that these features overlap with adjacent H_2O and CH_4 absorption bands which could create ambiguity when trying to derive chemical abundances from data with low spectral resolution. Therefore the optimal features that observations should focus on to differ an exoEarth from an

Table 1
Detecting Clear-sky ExoEarth Absorption Features

Feature	Wavelengths μm	Transits Required for Detection					
		0.4 ppm	4 ppm	40 ppm	400 ppm	4 k ppm	40 k ppm
$CH_4 + H_2O$	0.85–1.06	81	81	82	84	86	84
$CH_4 + H_2O$	1.08–1.24	25	25	25	25	26	25
$CH_4 + H_2O$	1.28–1.58	17	17	17	18	17	15
$CH_4 + H_2O$	1.59–2.0	9	9	9	9	9	8
CO_2	2.0–2.13	…	…	…	…	49	26
CH_4	2.15–2.48	7	7	7	7	8	8
$H_2O + CO_2$	2.5–3.0	11	11	12	11	10	8
CH_4	3.14–4.03	6	6	6	6	7	7
CO_2	4.11–4.45	18	17	16	14	11	9
$CO + N_2O$	4.46–5.0	28	28	28	29	30	29

Note. The dominant molecules and wavelength ranges for the 10 absorption features in the exoEarth spectra without clouds. The last six columns of the table list the number of transits needed to detect a given feature in each of the six exoEarth CO_2 cases. Dashes indicate the feature was unable to be detected in less than 100 transit observations.

Table 2
Detecting Cloudy ExoEarth Absorption Features

Feature	Wavelengths μm	Transits Required for Detection					
		0.4 ppm	4 ppm	40 ppm	400 ppm	4 k ppm	40 k ppm
$CH_4 + H_2O$	0.85–1.06	81	82	82	84	86	84
$CH_4 + H_2O$	1.08–1.24	25	25	25	25	26	25
$CH_4 + H_2O$	1.28–1.58	17	17	17	18	17	15
$CH_4 + H_2O$	1.59–2.0	9	9	9	9	9	8
CO_2	2.0–2.13	…	…	…	…	49	26
CH_4	2.15–2.48	7	7	7	7	8	8
$H_2O + CO_2$	2.5–3.0	11	11	12	11	10	8
CH_4	3.14–4.03	6	6	6	6	7	7
CO_2	4.11–4.45	18	17	16	14	11	9
$CO + N_2O$	4.46–5.0	28	28	28	29	30	29

Note. The dominant molecules and wavelength ranges for the 10 absorption features in the exoEarth spectra with clouds. The last six columns of the table list the number of transits needed to detect a given feature in each of the six exoEarth CO_2 cases. Dashes indicate the feature was unable to be detected in less than 100 transit observations.

Table 3
Detecting Clear-sky ExoVenus Absorption Features

Feature	Wavelengths μm	Transits Required for Detection					
		0.1%	0.5%	1%	25%	50%	96%
CO_2	1.16–1.4	…	…	…	…	…	…
CO_2	1.4–1.8	…	…	…	32	44	55
CO_2	1.83–2.25	89	39	30	15	19	25
CO_2	2.5–3.08	30	19	16	11	13	18
SO_2	3.9–4.11	52	47	47	63	…	…
CO_2	4.11–4.45	18	13	12	10	12	17
CO	4.46–5.0	93	62	55	38	52	71

Note. The dominant molecules and wavelength ranges for the 7 absorption features in the clear-sky exoVenus spectra. The last six columns of the table list the number of transits needed to detect a given feature in each of the six exoVenus CO_2 cases. Dashes indicate the feature was unable to be detected in less than 100 transit observations.

Table 4
Detecting Cloudy ExoVenus Absorption Features

Feature	Wavelengths μm	Transits Required for Detection					
		0.1%	0.5%	1%	25%	50%	96%
CO_2	1.16–1.4	…	…	…	…	…	…
CO_2	1.4–1.8	…	…	…	…	…	…
CO_2	1.83–2.25	…	…	…	…	…	…
CO_2	2.5–3.08	…	…	…	66	74	…
SO_2	3.9–4.11	…	…	…	…	…	…
CO_2	4.11–4.45	…	60	53	33	39	65
CO	4.46–5.0	…	…	…	…	…	…

Note. The dominant molecules and wavelength ranges for the seven absorption features in the hazy exoVenus spectra. The last six columns of the table list the number of transits needed to detect a given feature in each of the six exoVenus CO_2 cases. Dashes indicate the feature was unable to be detected in less than 100 transit observations.

exoVenus are those that are unique to either exoVenus or exoEarth spectra and have little overlap with other features.

The sole exoVenus absorption feature that cannot also be found in the exoEarth spectra is the SO_2 feature at 4 μm. Detection of SO_2 in atmospheric spectra could be indicative of a dry atmosphere since SO_2 is reactive with water vapor, which would inherently rule out the possibility of the planet being Earthlike. Present-day Venus has a dry atmosphere but has reduced amounts of SO_2 due to photochemical oxidation caused by UV radiation from the Sun. The hypothetical exoVenus in this work orbits TRAPPIST-1, and the reduced UV output from TRAPPIST-1 allows SO_2 to have an extended

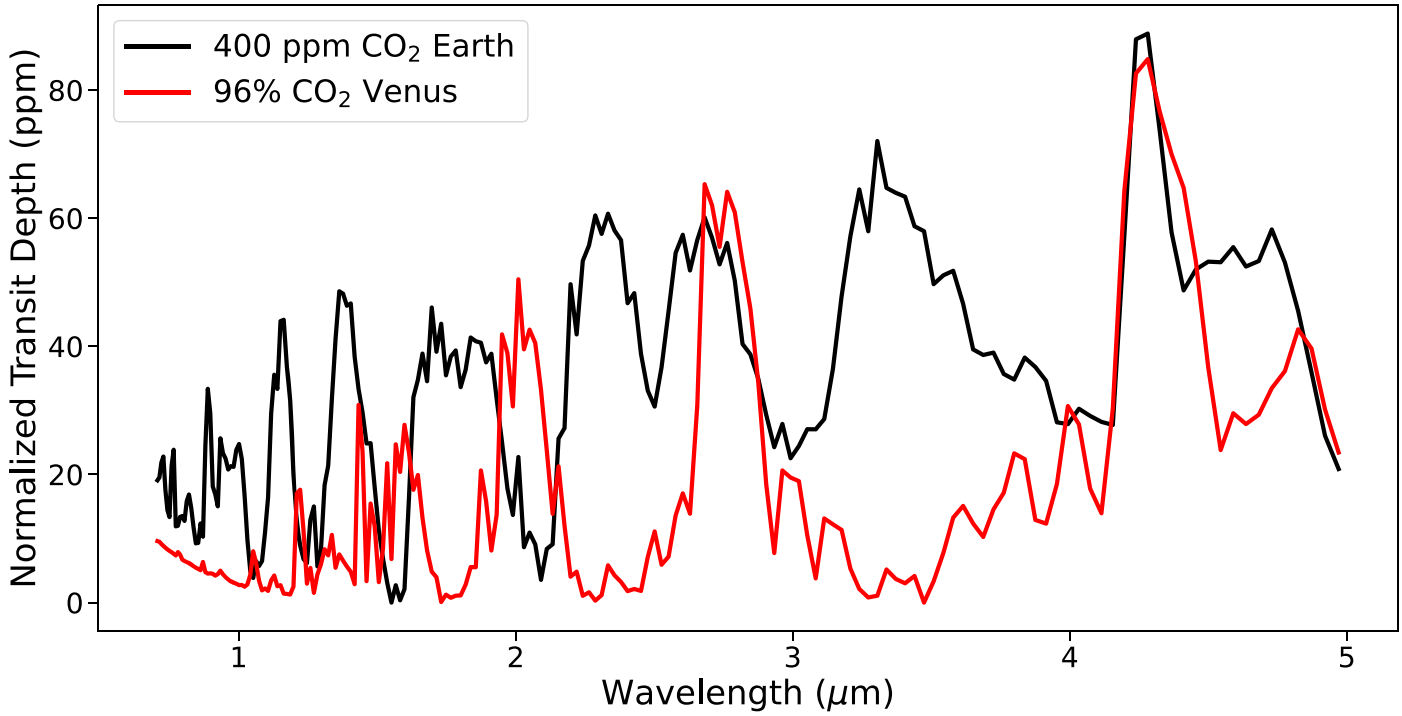

Figure 9. The transmission spectra of the 400 ppm CO_2 exoEarth and 96% CO_2 exoVenus. There are an abundance of absorption features which are unique to the exoEarth spectrum and could be used to differentiate it from an exoVenus. The exoVenus spectrum yields large CO_2 features at 1.7 and 2.0 μm; however, they may be difficult to resolve from adjacent H_2O absorption.

lifetime in the exoVenus atmosphere, which enhances the possibility of the SO_2 being detectable. Discovering SO_2 on a planet would provide insight into potential volcanism and tectonic activity occurring on the planet, both of which are vital for inferring climate conditions. In the clear-sky exoVenus spectra, the SO_2 feature can be detected in as little as 47 transits, and is undetectable in the 50% and 96% CO_2 cases (Table 3). In the hazy exoVenus spectra however, the SO_2 feature is undetectable in all CO_2 cases.

The majority of the CH_4 absorption features in the exoEarth spectra do not overlap with CO_2 features, and there are no CH_4 features present in the exoVenus spectra (Figure 9). Several H_2O features are also in the exoEarth spectra, but they all have significant overlap with adjacent CO_2 features. It has been well documented that detection of CH_4 and O_2 disequilibrium in an exoplanet atmosphere is a potential biosignatures for identifying habitable worlds (Lovelock 1965; Hitchcock & Lovelock 1967; Schindler & Kasting 2000; Des Marais et al. 2002; Kasting 2005; Arney et al. 2017; Krissansen-Totton et al. 2018; Thompson et al. 2022, e.g.,). Although CH_4 can contribute to a runaway greenhouse scenario (Pavlov et al. 2000; Haqq-Misra et al. 2008; Ramirez & Kaltenegger 2018), the likelihood of a detectable amount of CH_4 being produced from abiotic processes is far less likely than deriving from biotic processes (Guzmán-Marmolejo et al. 2013; Wogan et al. 2020, e.g.,), making it improbable to detect CH_4 on an exoVenus. These factors make CH_4 the optimal exoEarth absorption feature for discerning an exoEarth from an exoVenus.

The features at 0.9 and 1.1 μm in the exoEarth spectra are composed of both H_2O and CH_4 absorption (Table 1). These two features both have slight overlap with CO_2 features, but the CO_2 are much smaller than the H_2O features, even in cases of high CO_2 abundance (Figure 9). An additional observational benefit of the exoEarth features at 0.9 and 1.1 μm is that they are located at wavelengths where the NIRSpec PRISM has the highest spectral resolution Figure 8. Despite this, the 0.9 μ feature still requires at least 81 transit observations to be detected. The 1.1 μm feature proved to be far more detectable, requiring at most 26 transits in all exoEarth cases.

The feature at 1.8 μm, which is comprised of roughly equal parts CH_4 and H_2O absorption, and the CH_4 features at 2.3 and 3.5 μm are all very amenable to detection. All three features require at most nine transits to detect, and have minimal overlap with CO_2 features. As a result, these features are optimal for both minimizing observation time and clarifying that a planet is not Venus-like.

4.2. Observation Time

To put into perspective the amount of time needed to detect the features in the exoEarth and exoVenus transmission spectra, it is useful to compare the number of transits required for detection to the observation time criteria of JWST observing proposals. JWST proposals are separated into 3 categories based on the length of the observation. Small proposals are limited to 25 hr or less of total observing time, medium proposals range from 25 to 75 hr, and large proposals exceed 75 hr. A single transit observation in our JWST simulations equates to 1.75 hr since we assumed equal observing time in and out of transit. Cycle 2 JWST guest observer proposals assume an average slew time of 35 minutes, which would make a single transit observation equal to 2.33 hr when including overhead time. While considering slew time a small proposal could include at most 11 transit observations, 32 transits for a medium proposal, and more than 32 transits for a large proposal.

The only exoVenus features which could be detected within a small proposal are the 2.7 μm CO_2 feature in the 25% CO_2

case and the 4.3 μm CO_2 feature in the 1%, 25% and 50% cases. The time allotted by a medium proposal would be sufficient for detecting the 2.0 μ feature in the 3 highest CO_2 cases, and the 2.7 and 4.3 μm features in all cases. The 1.6 μm CO_2 feature can be detected in the 3 highest CO_2 cases in slightly more time than a medium proposal. The 4.0 μm SO_2 feature and 4.8 μm CO feature would both require a large proposal to be detected in all cases.

A small observing proposal for the exoEarth would be sufficient for detecting the CH_4 and H_2O features at 1.8, 2.3, 2.8, and 3.5 μm in all CO_2 cases, and the 4.3 μm CO_2 feature in the 4 k and 40 k ppm CO_2 cases. The only feature which would require a large proposal is the CH_4 feature at 0.9 μm, which would need far more transit observations than the minimum for a large proposal.

5. Conclusions

In this work we used VPL Climate to model the climate states and atmospheres of six hypothetical exoEarths and exoVenuses, all of which are located on the runaway greenhouse boundary in the TRAPPIST-1 system. Both the exoEarths and exoVenuses have varying abundances of atmospheric CO_2 that range from 0.4 to 40 k ppm CO_2 and 0.1%–96% CO_2, respectively. The atmospheres from the modeled planets were used as inputs for PSG to simulate their transmission spectra between 0.6 and 5.3 μm, including clear-sky and cloudy scenarios for both planets. The transmission spectra were then input into PandExo to simulate observations of the planets using JWST NIRSpec PRISM. Using the simulated JWST data we quantified the detectability of 10 absorption features in the clear-sky and cloudy exoEarth spectra, and seven features in the clear-sky and hazy exoVenus spectra. From this, we identified features in the spectra of both planets that would be useful for confirming whether a planet is Venus-like or Earthlike.

The SO_2 feature at 4.0 μm is the only feature unique to the exoVenus spectra, and the best opportunity to confirm a planet is more similar to Venus than Earth. The detectability of the SO_2 feature is volatile in clear-sky cases however, as it would require a minimum of 47 transits to detect in low CO_2 cases, and becomes undetectable with higher CO_2 abundance. When haze was included, the SO_2 feature was completely undetectable. The CO_2 features at 1.7, 2.0, and 2.7 μm are indicators for a CO_2 dense atmosphere; however, they will likely be difficult to discern from the adjacent H_2O and CH_4 features they overlap with, and are undetectable in hazy atmospheres.

The exoEarth has enhanced atmospheric CH_4 abundance because of the SED of its host star. As a result, the CH_4 features at 1.15, 1.8, 2.3, and 3.4 μm are all amenable to detection and are likely the best option in the NIR for ruling out a Venus-like planet. The presence of clouds had a minuscule effect on the detectability of features. Given that the exoVenus spectra only have a single unique absorption feature while the exoEarth spectra have several that are also far more detectable, it will likely be easier to confirm an exoEarth than it will be to confirm an exoVenus.

JWST is scheduled to observe several VZ planets in cycle 1, and will likely observe more in future cycles. These planets will serve as our first look into the climate conditions of planets with similar insolation flux as Venus, and will be a crucial resource for understanding the causes for Venus being inhospitable today. In addition, the discovery of habitable worlds in the VZ could strengthen the hypothesis that Venus could have had an extended temperate period in its past, and broaden the selection of planets that are targeted in search for signs of life. The importance of exoVenuses to the study of planetary habitability makes the ability to confidently identify Venus-like worlds paramount for maximizing what can be learned from observations of VZ planets with JWST NIRSpec and future facilities like the Extremely Large Telescope and the Habitable Worlds Observatory.

Acknowledgments

C.O. and S.R.K. acknowledge support from NASA grant 80NSSC21K1797, funded through the NASA Habitable Worlds Program, and also from NASA grant 80NSSC22M0188, funded through the NASA Discovery Program. P.D. is supported by a National Science Foundation (NSF) Astronomy and Astrophysics Postdoctoral Fellowship under award AST-1903811. A.P.L. was supported by the Virtual Planetary Laboratory Team, which is a member of the NASA Nexus for Exoplanet System Science, and funded via NASA Astrobiology Program grant 80NSSC18K0829. The results reported herein benefited from collaborations and/or information exchange within NASA's Nexus for Exoplanet System Science (NExSS) research coordination network sponsored by NASA's Science Mission Directorate. This work made use of the advanced computational, storage, and networking infrastructure provided by the Hyak supercomputer system at the University of Washington. The authors thank Dr. Tara Fetherolf and Dr. Kimberly Bott for their feedback, which helped improve the quality of this work.

Software: Planetary Spectrum Generator (Villanueva et al. 2018), PandExo: ETC for Exoplanets (Batalha et al. 2017).

ORCID iDs

Colby Ostberg https://orcid.org/0000-0001-7968-0309
Stephen R. Kane https://orcid.org/0000-0002-7084-0529
Andrew P. Lincowski https://orcid.org/0000-0003-0429-9487
Paul A. Dalba https://orcid.org/0000-0002-4297-5506

References

Arney, G., Meadows, V., Crisp, D., et al. 2014, JGRE, 119, 1860
Arney, G. N., Meadows, V. S., Domagal-Goldman, S. D., et al. 2017, ApJ, 836, 49
Barstow, J. K. 2020, MNRAS, 497, 4183
Barstow, J. K., Aigrain, S., Irwin, P. G. J., Kendrew, S., & Fletcher, L. N. 2016, MNRAS, 458, 2657
Batalha, N. E., Mandell, A., Pontoppidan, K., et al. 2017, PASP, 129, 064501
Cascioli, G., Hensley, S., De Marchi, F., et al. 2021, PSJ, 2, 220
Crisp, D. 1997, GeoRL, 24, 571
Crisp, D., & Titov, D. 1997, in Venus II: Geology, Geophysics, Atmosphere, and Solar Wind Environment, ed. S. W. Bougher, D. M. Hunten, & R. J. Phillips (Tucson, AZ: Univ. Arizona Press), 353
Des Marais, D. J., Harwit, M. O., Jucks, K. W., et al. 2002, AsBio, 2, 153
Ehrenreich, D., Tinetti, G., Des Etangs, A. L., Vidal-Madjar, A., & Selsis, F. 2006, A&A, 448, 379
Ehrenreich, D., Vidal-Madjar, A., Widemann, T., et al. 2012, A&A, 537, L2
Fauchez, T. J., Turbet, M., Villanueva, G. L., et al. 2019, ApJ, 887, 194
Felton, R. C., Bastelberger, S. T., Mandt, K. E., et al. 2022, JGRE, 127, e2021JE006853
Garvin, J. B., Getty, S. A., Arney, G. N., et al. 2022, PSJ, 3, 117
Ghail, R., Wilson, C., Widemann, T., et al. 2017, arXiv:1703.09010
Gordon, I. E., Rothman, L. S., Hill, C., et al. 2017, JQSRT, 203, 3
Greene, T. P., Bell, T. J., Ducrot, E., et al. 2023, Natur, 618, 39
Greene, T. P., Line, M. R., Montero, C., et al. 2016, ApJ, 817, 17

Guzmán-Marmolejo, A., Segura, A., & Escobar-Briones, E. 2013, AsBio, 13, 550
Hamano, K., Abe, Y., & Genda, H. 2013, Natur, 497, 607
Haqq-Misra, J. D., Domagal-Goldman, S. D., Kasting, P. J., & Kasting, J. F. 2008, AsBio, 8, 1127
Hitchcock, D. R., & Lovelock, J. E. 1967, Icar, 7, 149
Huang, X., Schwenke, D. W., Freedman, R. S., & Lee, T. J. 2017, JQSRT, 203, 224
Husser, T.-O., Wende-von Berg, S., Dreizler, S., et al. 2013, A&A, 553, A6
Kane, S. R., Arney, G., Crisp, D., et al. 2019, arXiv:1908.02783
Kane, S. R., Kopparapu, R. K., & Domagal-Goldman, S. D. 2014, ApJL, 794, L5
Kane, S. R., & von Braun, K. 2008, ApJ, 689, 492
Kasting, J. F. 2005, PreR, 137, 119
Komacek, T. D., Fauchez, T. J., Wolf, E. T., & Abbot, D. S. 2020, ApJL, 888, L20
Kopparapu, R. K., Ramirez, R., Kasting, J. F., et al. 2013, ApJ, 765, 131
Kopparapu, R. K., Ramirez, R. M., SchottelKotte, J., et al. 2014, ApJL, 787, L29
Krissansen-Totton, J., Olson, S., & Catling, D. C. 2018, SciA, 4, eaao5747
Lincowski, A. P., Meadows, V. S., Crisp, D., et al. 2018, ApJ, 867, 76
Lincowski, A. P., Meadows, V. S., Crisp, D., et al. 2021, ApJL, 908, L44
Louie, D. R., Deming, D., Albert, L., et al. 2018, PASP, 130, 044401
Lovelock, J. E. 1965, Natur, 207, 568
Lustig-Yaeger, J., Fu, G., May, E., et al. 2023, NatAs, in press
Lustig-Yaeger, J., Meadows, V. S., & Lincowski, A. P. 2019a, AJ, 158, 27
Lustig-Yaeger, J., Meadows, V. S., & Lincowski, A. P. 2019b, ApJL, 887, L11
Meadows, V. S., Arney, G. N., Schwieterman, E. W., et al. 2018, AsBio, 18, 133
Meadows, V. S., & Crisp, D. 1996, JGRE, 101, 4595
Meadows, V. S., Lincowski, A. P., & Lustig-Yaeger, J. 2023, PSJ, 4, 192
Ostberg, C., & Kane, S. R. 2019, AJ, 158, 195
Ostberg, C., Kane, S. R., Li, Z., et al. 2023, AJ, 165, 168
Pavlov, A. A., Kasting, J. F., Brown, L. L., Rages, K. A., & Freedman, R. 2000, JGRE, 105, 11981
Peacock, S., Barman, T., Shkolnik, E. L., Hauschildt, P. H., & Baron, E. 2019, ApJ, 871, 235
Pidhorodetska, D., Fauchez, T. J., Villanueva, G. L., Domagal-Goldman, S. D., & Kopparapu, R. K. 2020, ApJL, 898, L33
Pontoppidan, K. M., Pickering, T. E., Laidler, V. G., et al. 2016, Proc. SPIE, 9910, 991016
Ramirez, R. M., & Kaltenegger, L. 2018, ApJ, 858, 72
Ricker, G. R., Winn, J. N., Vanderspek, R., et al. 2015, JATIS, 1, 014003
Robinson, T. D., & Crisp, D. 2018, JQSRT, 211, 78
Robinson, T. D., Meadows, V. S., Crisp, D., et al. 2011, AsBio, 11, 393
Rothman, L. S., Gordon, I. E., Barber, R. J., et al. 2010, JQSRT, 111, 2139
Schindler, T. L., & Kasting, J. F. 2000, Icar, 145, 262
Stamnes, K., Tsay, S. C., Wiscombe, W., & Jayaweerz, K. 1988, ApOpt, 42, 2502
Stamnes, K., Tsay, S. C., Wiscombe, W., & Laszlo, I. 1988, DISORT, a general-purpose Fortran program for discrete-ordinate-method radiative transfer in scattering and emitting layered media: documentation of methodology, ftp://climate.gsfc.nasa.gov/pub/wiscombe/MultipleScatt/
Stassun, K. G., Oelkers, R. J., Paegert, M., et al. 2019, AJ, 158, 138
Thompson, M. A., Krissansen-Totton, J., Wogan, N., Telus, M., & Fortney, J. J. 2022, PNAS, 119, e2117933119
Turbet, M., Bolmont, E., Chaverot, G., et al. 2021, Natur, 598, 276
Villanueva, G. L., Smith, M. D., Protopapa, S., Faggi, S., & Mandell, A. M. 2018, JQSRT, 217, 86
Way, M., Ostberg, C., Foley, B. J., et al. 2023, SSRv, 219, 13
Way, M. J., & Del Genio, A. D. 2020, JGRE, 125, e06276
Way, M. J., Del Genio, A. D., Kiang, N. Y., et al. 2016, GeoRL, 43, 8376
Wilson, D. J., Froning, C. S., Duvvuri, G. M., et al. 2021, ApJ, 911, 18
Wogan, N., Krissansen-Totton, J., & Catling, D. C. 2020, PSJ, 1, 58
Zieba, S., Kreidberg, L., Ducrot, E., et al. 2023, Natur, 620, 746